Effect of Pick Spacing and Warp and Weft Volume Fraction on Intrinsic Residual Stresses in 3D Woven Composites

TODD GROSS, HILARY BUNTROCK,
KOSTIANTYN VASYLEVSKYI, IGOR TSUKROV
and BORYS DRACH

ABSTRACT

Three panels of 3D woven carbon fiber/RTM6 epoxy composites with a ply-to-ply weave with 12x12 (warp/weft) picks per inch (ppi), 10x12 ppi, and 10x8 ppi were fabricated by resin transfer molding. Realistic finite element models of each weave architecture were constructed using Dynamic Fabric Mechanics Analyzer. The resin properties were isotropic and linear elastic and dependent on temperature. The resin-infiltrated fiber tow properties were estimated using homogenization based on Hashin and Shapery formulas. The model was considered to be at zero stress at the 165°C curing temperature. The stresses resulting from cooling the composite to 25°C were estimated using the resin temperature-dependent properties and the temperature independent properties of the tows. The displacement fields resulting from holes drilled through the middle of the top warp or weft yarn were estimated by virtually drilling a hole in the finite element model and were measured on the specimens using electronic speckle pattern interferometry. In general, the measured displacements transverse to the yarn were lower than the predicted displacements. This suggests the resin in the infiltrated yarns relieves some of the stress by permanently deforming during cooling. The measured displacements along the yarn were approximately the same for the 12x12 ppi,, lower for the 10x12 ppi, and significantly higher for the 10x8 ppi.

Todd. Gross, Hilary Buntrock, Igor Tsukrov, Kostiantyn Vasylevskyi, University of New Hampshire, Department of Mechanical Engineering 33 Academic Way, Durham, NH 03824, U.S.A..
Borys Drach, New Mexico State University, Department of Mechanical and Aerospace Engineering, P.O. Box 30001, MSC 3450, Las Cruces, NM 88003-8001, U.S

INTRODUCTION

The coefficient of thermal expansion mismatch between epoxy resins and carbon fibers leads to a spatially varying internal residual stress field that increases in magnitude as the composite cools from the curing temperature. This intrinsic residual stress field has periodicity corresponding to the repeating unit cell of the composite. The fibers in resin-impregnated fiber tows will generally experience compressive residual stress and the resin in the fiber tows and between the fiber tows will experience a tensile residual stress. The magnitude of these stresses in a given architecture will necessarily depend on the volume fraction of fiber tows and is sometimes sufficient to cause microcracking in the composite.

We have developed techniques to create realistic finite element models of 3D woven architectures and subject those models to the temperature change resulting from cooling from the curing temperature to room temperature to estimate the intrinsic residual stress field. These models are used to evaluate the impact of changing weave architecture and yarn volume fraction on the intrinsic residual stress. One way to evaluate the accuracy of the model predictions is to experimentally measure the displacement fields resulting from drilling holes at selected locations in the composite and compare those measurements to predictions of the displacement field from virtually drilling a hole in the model.

The goal of this work is to compare the prediction of surface displacement fields to experimentally measured surface displacement fields in three ply-to-ply architectures with differing volume fractions of warp and weft fibers.

METHODS

Experimental Methods

Three panels of 4.1 mm thickness were fabricated by Albany Engineered Composites using Hexcel RTM6 resin and Hexcel 12K IM7 PAN-based carbon fibers. All panels had the ply-to-ply architecture (shown in Figure 1) and had in-plane unit cell dimensions of 10.16 mm by 10.16 mm. Each panel had different overall volume fraction of fiber and different number of warp and weft picks-per-inch (ppi). The details of each panel are summarized in Table 1.

Sections that contained at least nine unit cells were cut out from the panels and painted first with white, high heat spray paint and then covered with a clear matte spray paint to protect the surface from drilling debris. The sample was glued on a block mounted on a Thor Labs kinematic mount to allow precise repositioning between the before drilling and after drilling. The apparent placement repeatability was on the order of 5 μm or less

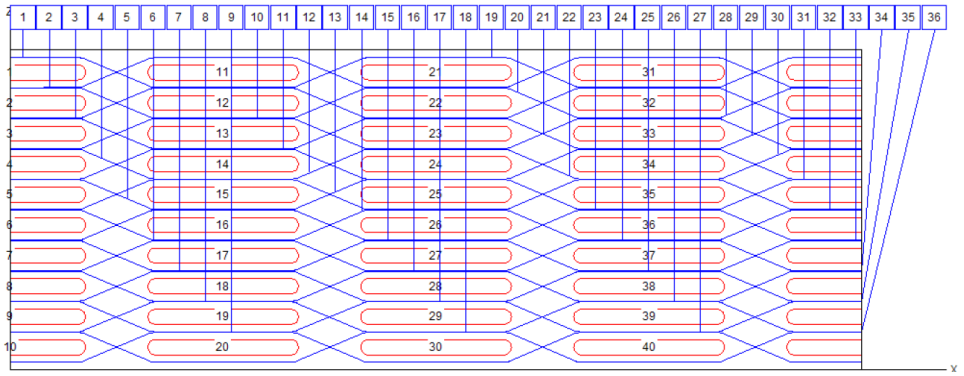

Figure 1. Ply-to-ply weave architecture.

Drilling the 1 mm diameter holes was accomplished with UKAM diamond coring tool. The depth of 0.3 mm was selected to just cut through the top yarn on the surface and not into the yarn below. The depth was measured with a dial indicator attached to the drilling head. A continuous flow of deionized water was manually applied during drilling using a squeeze bottle. The water was used to minimize the heat generated during drilling and to carry away the drilling debris. The sample was rinsed with more water after drilling and dried with a flow of warm air.

We used a custom-built electronic speckle pattern interferometry system similar to the one described by Diaz et al [1] to determine the in-plane displacements outside the high displacement gradient region near the hole. A diagram of the system is shown in Figure 2. We used a 50 mW Melles Griot HeNe laser that had linear polarization. The angle between the normal to the specimen and the illumination beams was 45° which results in a 448 nm displacement for a phase difference corresponding to 2π. Our system exhibited phase noise of $<\pi/25$ which corresponds to a displacement of 9 nm. A picture frame region around the edge of the image was used to correct for any displacements from repositioning the sample on the holder or from small amounts of thermal expansion (which would result in a linearly changing displacement across the image).

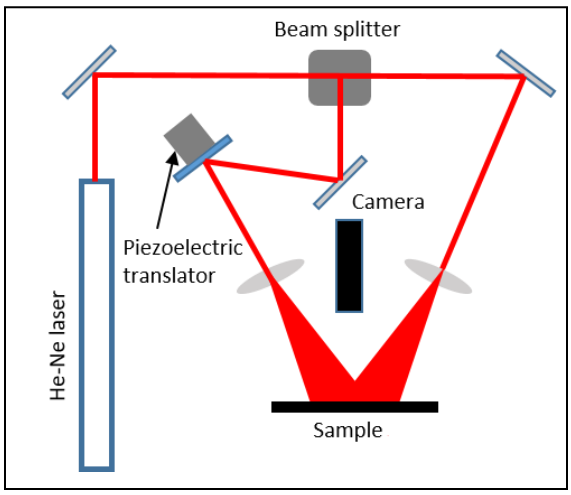

Figure 2. Electronic speckle pattern interferometry setup.

Computational methods

A realistic geometric model of the weave architectures was constructed using Dynamic Fabric Mechanical Analyzer (DFMA) (see [2], [3]). This software models digital fibers as digital rod elements connected with flexible links and contact elements. The digital fibers are combined into yarns where all fibers have the same length. The volume occupied by one digital fiber would be filled by multiple actual fibers. One can then specify the number of digital fibers per yarn and whether the fibers in the yarn are straight or twisted. The yarns are assembled into an expanded representation of the unit cell topology and the final unit cell is determined from a dynamic relaxation approach. The surface of each yarn in the final structure is exported as a point cloud used to create the finite element mesh of the unit cell using a custom Matlab script. All model preparation steps are performed automatically within the MSC Mentat software using a custom Python script.

TABLE I. VOLUME FRACTION CALCULATED FROM DFMA (AS-FABRICATED VALUES).

Picks-per-inch (warp x weft)	$\mathbf{V_{f\text{-}warp}}$	$\mathbf{V_{f\text{-}weft}}$	$\mathbf{V_f}$
12 x 12	0.35 (0.37)	0.39 (0.41)	0.74
10 x 12	0.23 (0.33)	0.46 (0.33)	0.69
10 x 8	0.35 (0.30)	0.28 (0.26)	0.62

The volumetric mesh for the tows is generated using Marc Mentat based on the surface mesh for the yarns in the unit cell. The volumetric mesh for the resin is also generated in Marc Mentat by changing the sign of the normal vector to the surface mesh of the yarn. Custom scripts are used to improve the surface mesh at the lateral boundaries of the unit cell so that the mesh of the unit cell is rigorously/exactly congruent (nodal pattern is the same). More details of this process can be found in [4]. There are areas of penetration between adjacent tows that are corrected manually and using custom scripts. This results in differences between the model and the tow volume fraction used to fabricate the specimens. This difference is greatest for the 10 x 12 architecture.

The properties of the RTM6 epoxy matrix are assumed to be homogeneous and isotropic. The Young's modulus, E, and coefficient of thermal expansion, α, depend on temperature as:

$$E_m = E_m^{0^o C} - \beta_m T$$
$$\alpha_m = \alpha_m^{0^o C} + \gamma T \qquad (0.1)$$

where $E_m^{0^o C} = 350\,MPa, \beta_m = 5.9\frac{MPa}{^oC}$, $\alpha_m^{0^o C} = 5 \bullet 10^{-5}\frac{1}{K}$, *and* $\gamma_m = 1.05 \bullet 10^{-7}\frac{1}{K}$ and T is in °C.

The yarns are modeled as a transversely isotropic material that represents the resin impregnated 12K carbon fibers assuming an 80% volume fraction of fibers within the yarns. The effective properties are estimated using micromechanical models of Hashin and Shapery [5], [6] for continuous unidirectional composites. as. E_{1t} = 221.38 GPa, E_{2t} = 13.18 GPa, $G1_{2t}$ = 7.17 GPa, v_{12t} = 0.35, v_{23t} = 0.35, $\alpha_{1t} = -2.29 \cdot 10 - 7\ K^{-1}$, $\alpha_{2t} = 2.23 \cdot 10^{-5}\ K^{-1}$. In these expressions, direction 1 is parallel to the axis of the yarn and directions 2 and 3 are transverse to the yarn axis. Note that even though the

properties of the matrix in the tows change with temperature as given by (1.1), these changes will result in insignificant variations of the homogenized properties of the tows (see comparison in [7]), so in the numerical simulations the properties of the tows are assumed to be temperature independent.

The hole drilling was simulated using Marc Mentat's capability to deactivate elements. First, the simulation of the cooling after curing was performed assuming that the temperature of the completely cured composite panel uniformly changes from 185°C to 25°C while lateral surfaces of a unit cell stay periodic but are allowed to move laterally to accommodate the overall shrinkage of the composite panel. Then the elements corresponding to the position of the hole were manually selected to deactivate. Subtracting the displacements obtained after the simulation of curing from the displacements after removing the elements representing the hole produces the displacement field from the hole drilling. Figure 3 shows the finite element model and the region where the nodes were deactivated to simulate drilling of the hole.

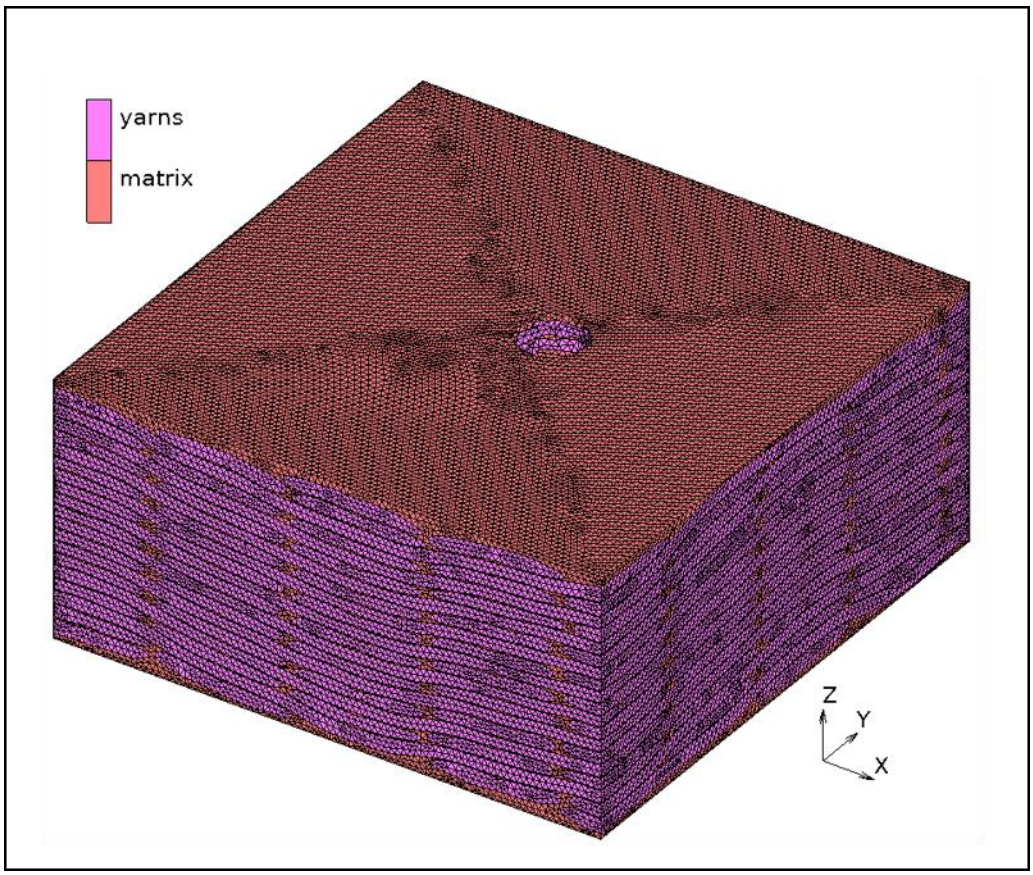

Figure 3. Finite element model showing region where hole was virtually drilled.

RESULTS AND DISCUSSION

The results follow the convention that the warp are parallel to the horizontal (x, u) direction and the weft fibers are parallel to the vertical (y, v) direction. All stress estimates are based on the volume fraction estimated using the DFMA model. We estimated the average stress in the volume of material occupied by the hole for each sample. The results are summarized in Figure 4. As can be seen, the stresses are compressive along the yarn axis and tensile transverse to the yarn axis.

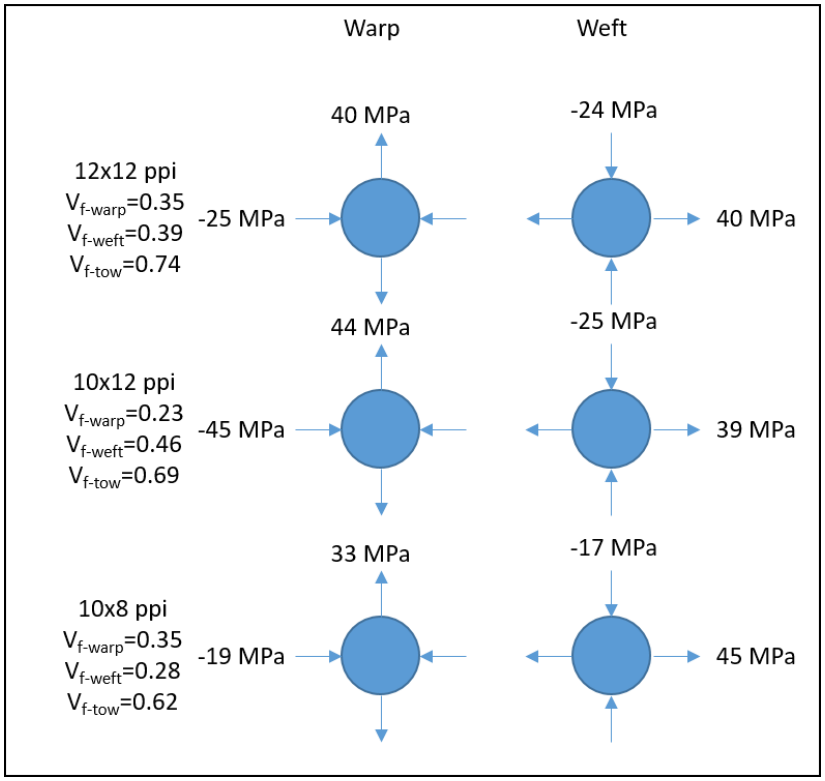

Figure 4. Average stresses integrated over the volume of the material removed by drilling. The shear stresses were all much smaller.

The stresses along the fiber axis are plotted vs. volume fraction along the axis of the tow in Figure 5. The magnitude of the stresses in the warp tows decrease with increasing volume fraction of warp tows which is consistent with the thermal mismatch strain being distributed in a larger volume of fibers. However, the magnitude of the stresses in the weft fibers slightly increases with increasing volume fraction. We have no explanation for the trend of stress for the weft tows at this time.

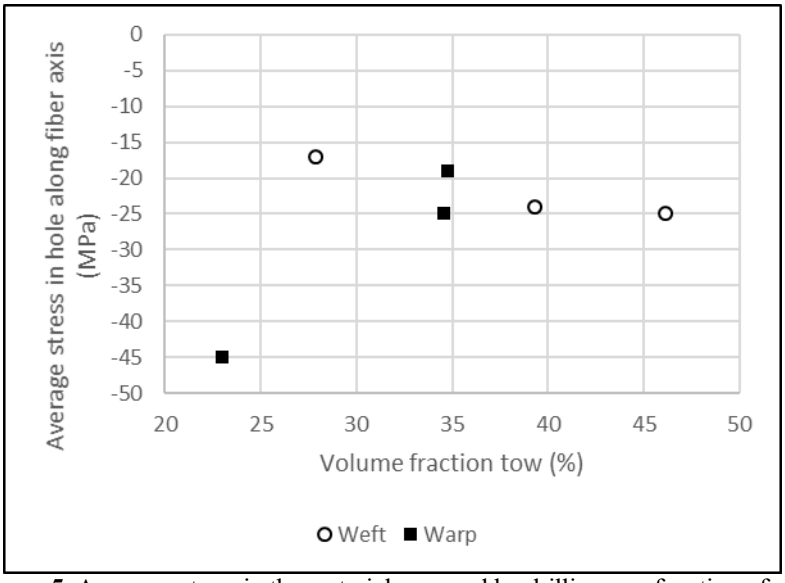

Figure 5. Averages stress in the material removed by drilling as a function of warp or weft volume fraction.

The predicted and experimentally obtained displacement fields will be presented for holes in the warp and weft tows for each architecture. The displacements are encoded as shades of blue for negative displacements and shades of red for positive displacements. The magnitude of the predicted displacements was often greater than the observed displacements so the color range corresponds to ±2500 nm for the predicted displacements and ±500 nm for the observed displacements. Slices through the center of the hole in the direction of maximum observed displacement are provided for each hole to compare the magnitude of the displacements.

The results for the holes in the warp tows in the 12x12, 10x12, and 10x8 ppi structures are shown in Figure 6, Figure 7, and Figure 8. The predicted displacements along the warp tow axis (u direction) are outward along the tow axis very near to the hole but toward the hole in the far-field region. These near-field displacements are not consistent with the predicted state of compressive stress in the tows, but the far-field displacements are. The observed displacements along the tow axis are toward the hole for the entire field and have roughly the same shape as the far-field displacement predictions. The displacement magnitude is approximately the same in the far field region for the 12x12 and 10x12 ppi structures but begins to deviate in the region where the predicted displacements change sign near the edge of the hole. The displacement magnitude observed for the 10x8 structure is ~2x greater than observed for the 12x12 and 10x12 structure as well as being greater than the prediction.

One possible explanation for why the near-field opposite sign displacement region is predicted along the tow axis for warp and weft tows but not observed is that the model has a larger overburden of resin than the specimen. The resin overburden is under biaxial tensile stress. The spatial resolution of the experimental method is <30 μm and the near-field, opposite signed displacements are over a ~500 μm region near the hole. So, it is unlikely that the technique missed these displacements if they were present. Future work will investigate the impact of differing overburdens of resin on the displacement field from hole drilling.

The predicted and observed displacements transverse to the warp tow axis (v direction) in the 12x12 and 10x12 ppi panel are both away from the hole although the

observed displacements are 4-5x lower than the predicted displacements. The shape of the predicted and observed fields is roughly the same. The predicted and observed displacements transverse to the warp tow in the 10x8 ppi structure also have the same shape but are nearly the same magnitude as the prediction. This is the only hole out of six where the observed transverse displacements are nearly the same. The observed transverse displacements for the remaining are typically 4-5x lower than the prediction. We propose that the resin in the tow deforms by inelastic (plastic, viscoelastic, or viscoplastic) deformation during cooling and relieves the stresses.

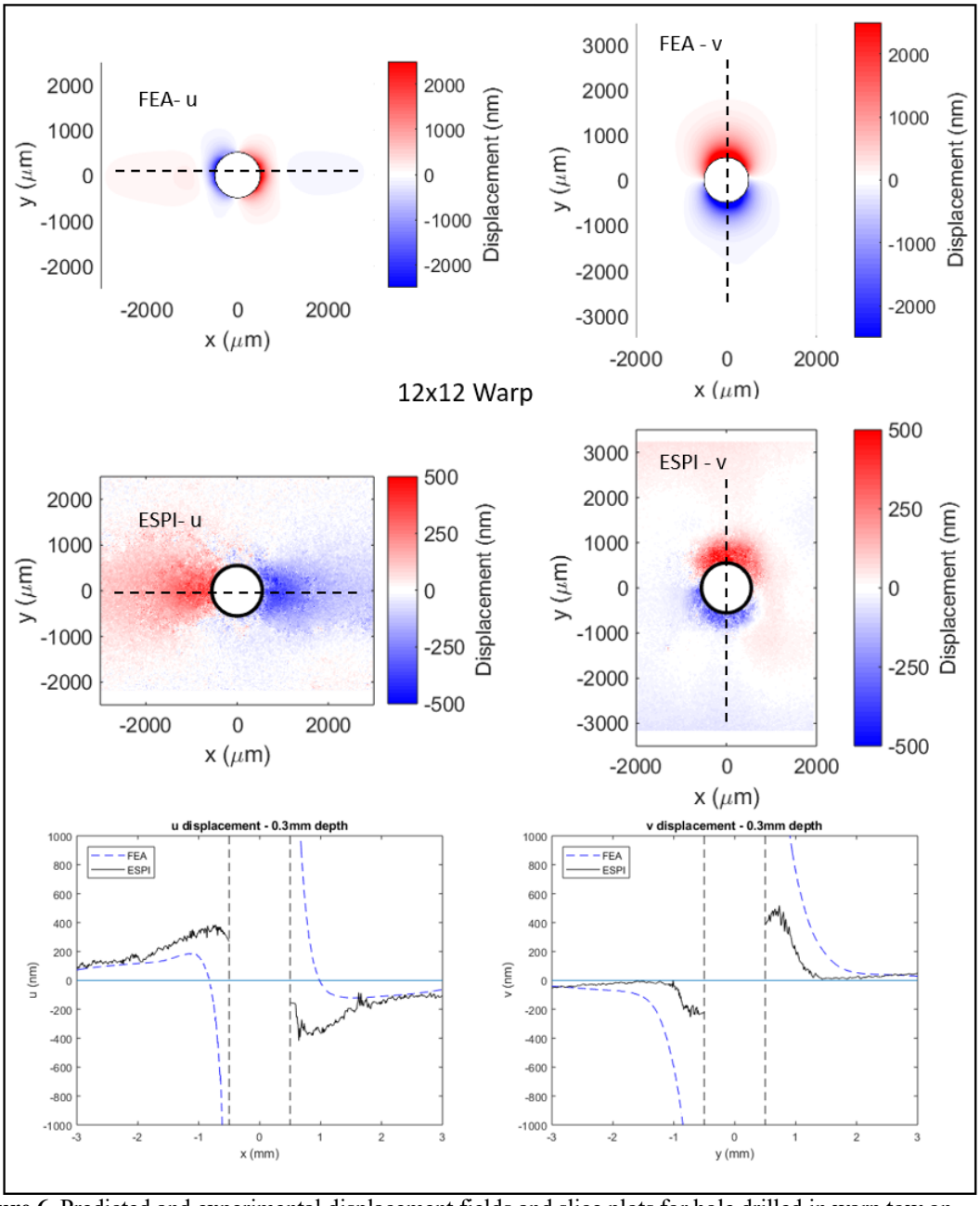

Figure 6. Predicted and experimental displacement fields and slice plots for hole drilled in warp tow on 12x12 ppi structure. The u displacements are horizontal and in the warp direction. The v displacements are in the vertical direction and transverse to the tow. Note that the displacement scale for the FE results is 5 times that for the experimental results.

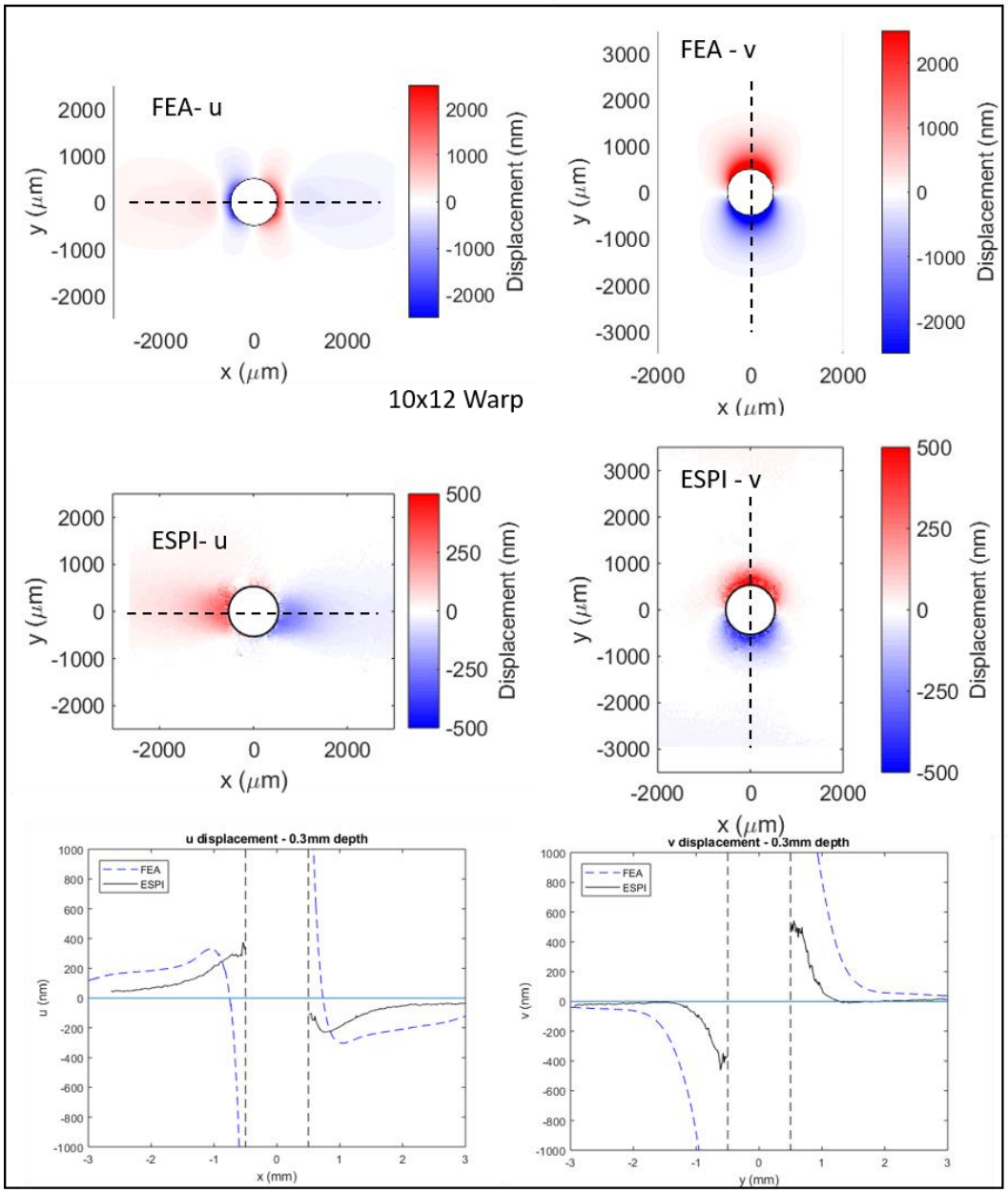

Figure 7. Predicted and experimental displacement fields and slice plots for hole drilled in warp tow on 10x12 ppi structure. The u displacements are horizontal and in the warp direction. The v displacements are in the vertical direction and transverse to the tow. Note that the displacement scale for the FE results is 5 times that for the experimental results.

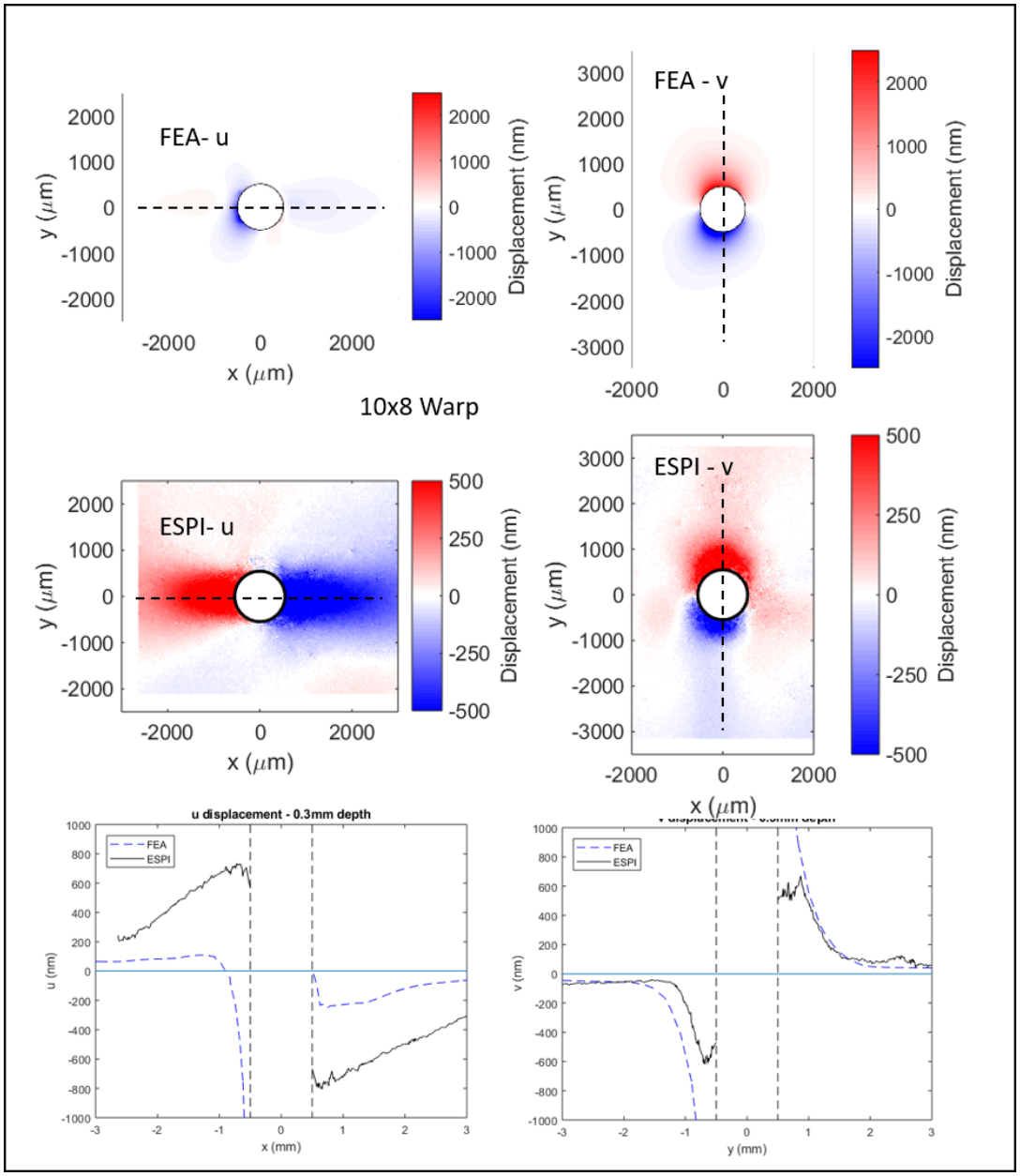

Figure 8. Predicted and experimental displacement fields and slice plots for hole drilled in warp tow on 10x8 ppi structure. The u displacements are horizontal and in the warp direction. The v displacements are in the vertical direction and transverse to the tow. Note that the displacement scale for the FE results is 5 times that for the experimental results.

The predicted and observed displacements for the weft tows are shown in Figure 9, Figure 10, and Figure 11. As mentioned above, the magnitude of the displacements transverse to the tow axis (u direction) are 4-5x lower than the prediction. The shape of the predicted and observed displacement field transverse to the tow axis are also very similar.

The observed far-field displacement field along the weft tow axis are roughly the same as the prediction for the 12x12 and 10x12 ppi structure but the opposite signed near-field displacements are not observed. The observed weft displacement field along the tow axis for the 10x8 ppi structure has different shape and is opposite in sign. The magnitude of the displacements along the weft tow is slightly lower than along the warp tow in the 10x8 structure.

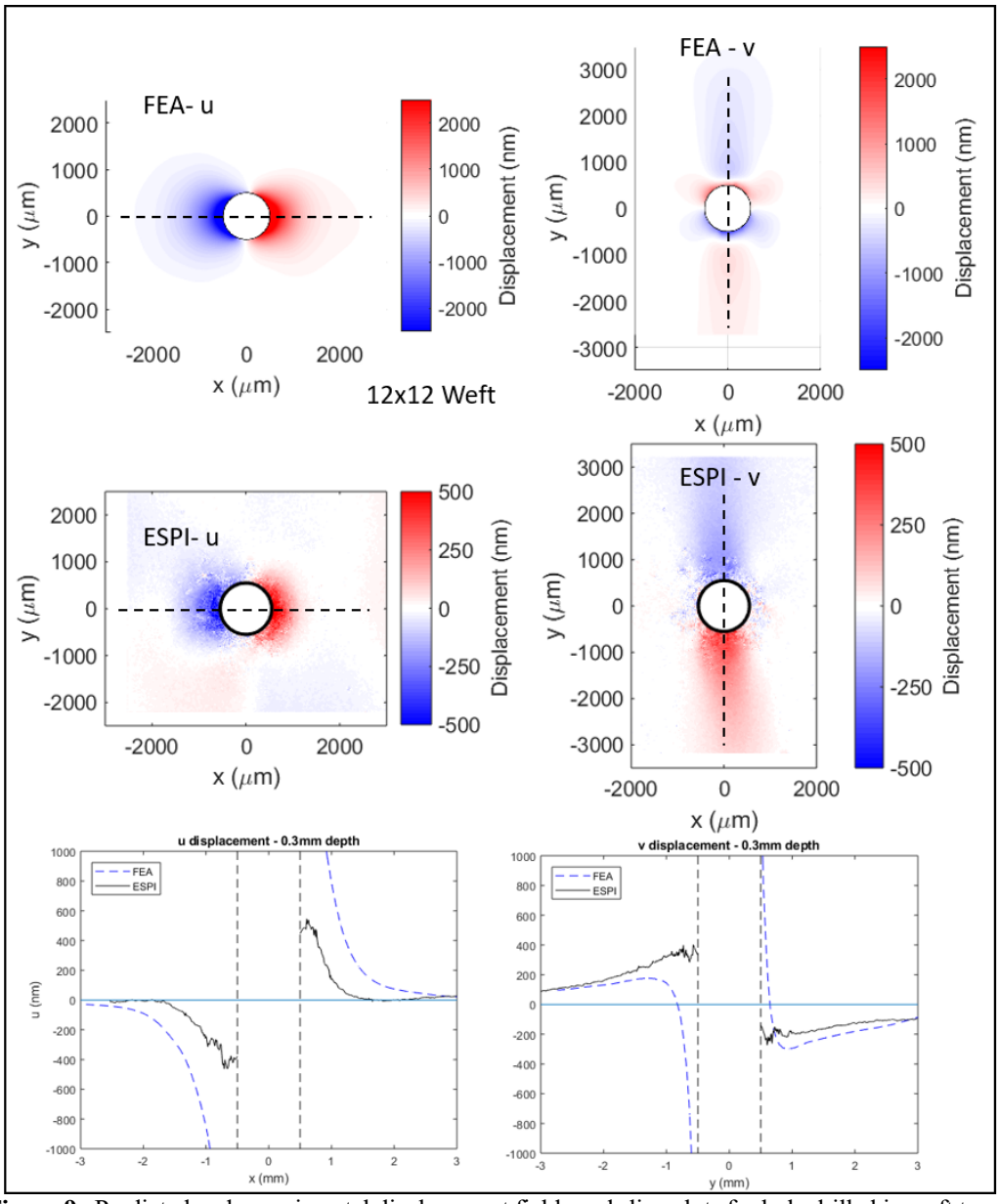

Figure 9. Predicted and experimental displacement fields and slice plots for hole drilled in weft tow on 12x12 ppi structure. The u displacements are horizontal and in the warp direction. The v displacements are in the vertical direction and transverse to the tow. Note that the displacement scale for the FE results is 5 times that for the experimental results.

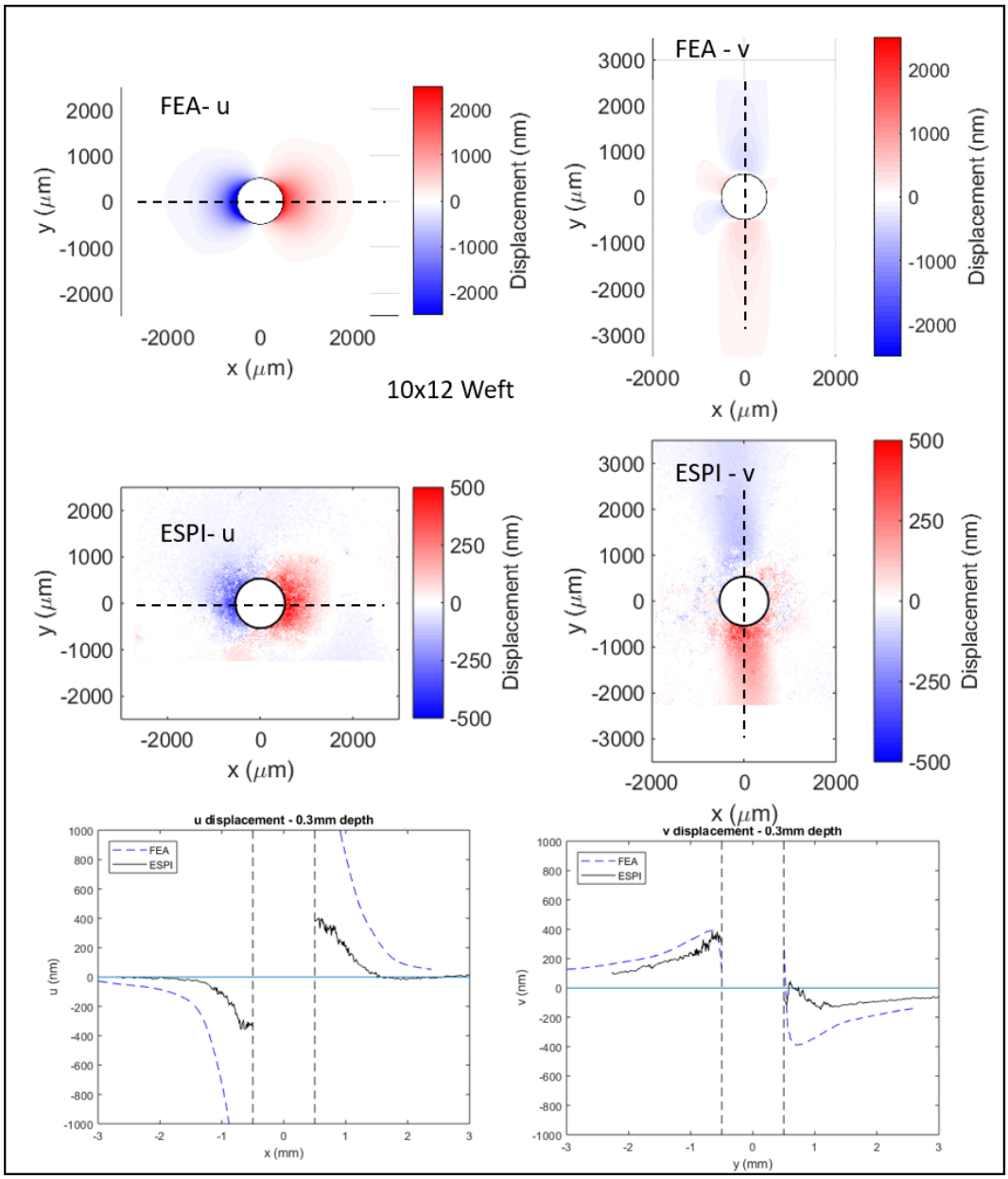

Figure 10. Predicted and experimental displacement fields and slice plots for hole drilled in weft tow on 10x12 ppi structure. The u displacements are horizontal and in the warp direction. The v displacements are in the vertical direction and transverse to the tow. Note that the displacement scale for the FE results is 5 times that for the experimental results.

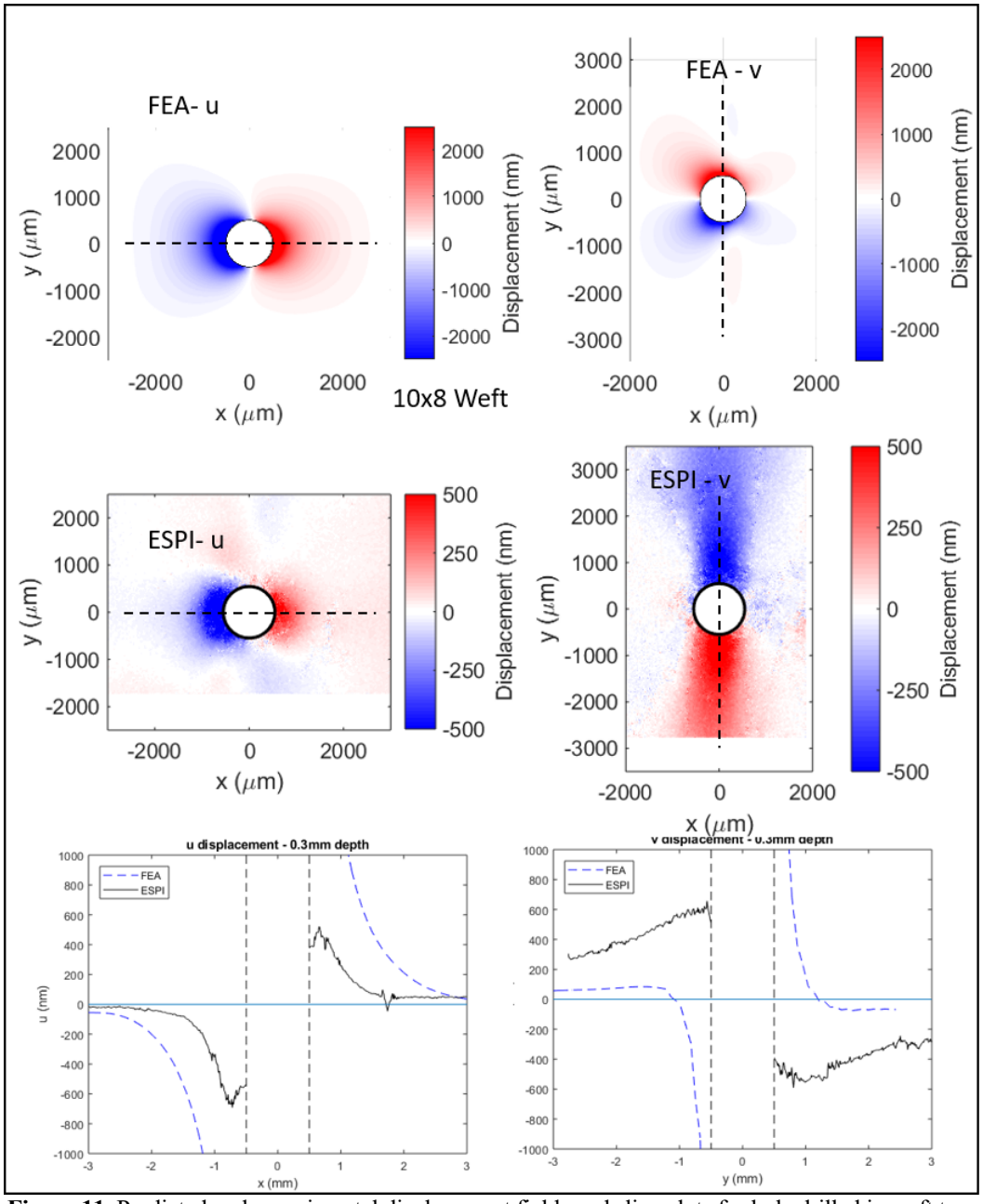

Figure 11. Predicted and experimental displacement fields and slice plots for hole drilled in weft tow on 10x8 ppi structure. The u displacements are horizontal and in the warp direction. The v displacements are in the vertical direction and transverse to the tow. Note that the displacement scale for the FE results is 5 times that for the experimental results.

SUMMARY AND CONCLUSIONS

We compared the predicted and observed displacement fields for holes drilled through the top warp and weft yarns in ply-to-ply 3D woven panels prepared with 12x12, 10x12, and 10x8 picks per inch to evaluate the accuracy of the finite element models and to quantify the intrinsic residual stress field. The intrinsic residual stresses are caused by mismatch in thermal expansion coefficient between the resin and the fibers during cooling from the curing temperature. For all holes, the shape of the displacement fields transverse to the tow axis were very similar. For all but one hole, the magnitudes were 4-5x lower than the predictions. This strongly suggests that the stresses in the tow are relieved by inelastic deformation of the matrix during cooling. The predicted shapes of the displacement fields along the tow axis all had a near-field region that suggested local tensile stresses instead of the expected compressive stresses exhibited by the far-field displacements. This is attributed to local relaxation of the thicker resin overburden in the model than the specimen. The magnitude of the far-field displacements was roughly the same for three of the six holes. The 10x8 ppi structure exhibited the most deviation from the predictions.

ACKNOWLEDGEMENTS

This work was supported by a grant CMMI-1662098 from the National Science Foundation, Civil, Materials, and Manufacturing Innovation, Division of Materials Engineering and Processing. The sample preparation from Albany Engineered Composites is also gratefully acknowledged.

REFERENCES

[1] F. V Diaz, G. H. Kaufmann, and G. E. Galizzi, "Determination of residual stresses using hole drilling and digital speckle pattern interferometry with automated data analysis," *Opt. Lasers Eng.*, vol. 33, no. 1, pp. 39–48, 2000.

[2] Y. Wang and X. Sun, "Digital-element simulation of textile processes," *Compos. Sci. Technol.*, vol. 61, pp. 311–319, 2001.

[3] Y. Miao, E. Zhou, Y. Wang, and B. Cheeseman, "Mechanics of textile composites: microgeometry," *Compos. Sci. Technol.*, vol. 68, pp. 1671–1678, 2008.

[4] A. Drach, B. Drach, and I. Tsukrov, "Processing of fiber architecture data for finite element modeling of 3D woven composites Dedicated to Professor Zdeněk Bittnar in occasion of his 70th birthday.," *Adv. Eng. Softw.*, vol. 72, pp. 18–27, 2014.

[5] Z. Hashin, "Analysis of properties of fiber composites with anisotropic constituents," *J. Appl. Mech.*, vol. 46, pp. 543–550, 1979.

[6] R.S. Schapery, "Thermal expansion coefficients of composite materials based on energy principles," *J. Compos. Mater.*, vol. 2, pp. 380–404, 1968.

[7] B. Drach, I. Tsukrov, A. Trofimov, T. Gross, and A. Drach, "Comparison of stress-based failure criteria for prediction of curing induced damage in 3D woven composites," *Compos. Struct.*, vol. 189, 2018.